Precision Engineering 46 (2016) 221–231

Contents lists available at ScienceDirect

Precision Engineering

journal homepage: www.elsevier.com/locate/precision

A planar 3-DOF nanopositioning platform with large magnification

Ruizhou Wang, Xianmin Zhang*

Guangdong Provincial Key Laboratory of Precision Equipment & Manufacture Technology, South China University of Technology, 510641 Guangzhou, China

ARTICLE INFO

Article history:
Received 1 June 2015
Received in revised form 15 March 2016
Accepted 30 April 2016
Available online 3 May 2016

Keywords:
Nanopositioning
Large magnification
Displacement loss
Preload
Micro/nano manipulation

ABSTRACT

Piezo-actuated flexure-based precision positioning platforms have been widely used in micro/nano manipulation. A conventional major challenge is the trade-off between high rigidity, large magnification, high-precision tracking, and high-accuracy positioning. A compact planar three-degrees-of-freedom (3-DOF) nanopositioning platform is described in which three two-level lever amplifiers are arranged symmetrically to achieve large magnification. The parallel-kinematic configuration with optimised sizes increases the rigidity. Displacement loss models (DLM) are proposed for the external preload port of the actuator, the input port of the platform and the flexible lever mechanism. The kinematic and dynamic modelling accuracies are improved by the compensation afforded by the three DLMs. Experimental results validate the proposed design and modelling methods. The proposed platform possesses high rigidity, large magnification, high-precision circle tracking and high-accuracy positioning.

1. Introduction

Planar nanopositioning platforms play a crucial role in precise and accurate nanoscale positioning. The applications involve precision mechanical scanning in scanning probe microscopy (SPM) [1–5], nanoimprint lithography [6,7], micro-/nano manipulation [8–10], and micro-/nano surface metrology measurement [11]. Compared to a two-degrees-of-freedom (2-DOF, x & y) positioning platform [1,4,5], the planar 3-DOF platform increases the DOF and is capable of correcting possible undesired coupling between major axes. The serial-kinematic planar 3-DOF platform has a large workspace, good dexterity, decoupling, linear kinematic, and simple forward kinematic [2,12–14]. The parallel-kinematic configuration has high structural stiffness, high precision, low inertia, and wide bandwidth. The parallel structure combined with equilateral symmetry and planar geometry limits the thermal drift in position and orientation. For micro-/nano manipulation, a conventional major challenge is the trade-off between high rigidity, large magnification, high-precision tracking, and high-accuracy positioning. The parallel configuration has much more potential [6,9–11,15–19]. Planar parallel 3-DOF nanopositioning platforms have been widely used in wafer positioning [6,7], optical alignment [20], and micro/nano manipulation [9].

The traditional configuration of precision positioning platforms consists of one or more revolute, prismatic or sliding joints. Such joints always bring about backlash, friction, stick-slip, noise, or slow response. To achieve a high positioning accuracy, flexure hinges are used to replace traditional kinematic pairs [21,22]. Compliant mechanisms can be modelled using the pseudo-rigid-body model (PRBM) approach. This method assumes that the flexure hinges behave as revolute joints with torsional springs, and that the thicker sections of the mechanism act as rigid links. This enables the traditional optimal design method for planar 3-DOF parallel platforms to be applied, in which the global conditioning index, stiffness index, payload index and velocity index are used [23,24].

The piezoelectric ceramic actuator (PCA) gives sub-nanometer resolution, high generated force, wide dynamic response range and rapid motion, without mechanical play or wear. A widely-used type of PCA is the packaged PCA (PPCA) fabricated as multiple-layer piezoelectric stacks protected by a case. The internal preload makes the stacks ideal for dynamic applications, as well for tensile loads. The strain gauge sensor (SGS) embedded in the PPCA is used to measure the nominal displacement of all the stacks. A controller using data from the SGS has been developed to overcome hysteresis, creep and nonlinearity of the piezoelectric actuator [25]. The controller is a semi-closed-loop controller for the whole platform; however, actual input displacement of the platform differs from the nominal displacement of the PPCA, due to the external preload stiffness of the PPCA and the input stiffness of the platform. The displacement loss model (DLM) for the external preload port of the PPCA and the input port of the platform were important factors that needed to be considered. In particular, for

* Corresponding author at: Building No. 19, South China University of Technology, Wushan Road, Tianhe District, China. Tel.: +86 02087110059.
E-mail addresses: w.ang.rz@163.com (R. Wang), zhangxm@scut.edu.cn (X. Zhang).

http://dx.doi.org/10.1016/j.precisioneng.2016.04.016

Nomenclature

$\boldsymbol{F}$	system force matrix
$\boldsymbol{K}$	system stiffness matrix
$\boldsymbol{x}$	system displacement vector
J	forward-kinematic Jacobian matrix
ϕ	center of the hinge, $\phi \in \{k, a, b, c, A, B, C\}$
$\phi_i\varphi_i$	link between ϕ_i and φ_i, $\varphi \in \{k, a, b, c, A, B, C\}$.
ψ	link or moving plate, $\psi \in \{a_ib_i, b_ic_i, A_iB_i, B_iC_i, p\}$
θ	rotational angle along z axis
x, y, z	reference axes, deflections
δ_{ϕ_i}	equivalent translational displacement of ϕ_i
δ_{PPCA}	nominal displacement of the PPCA
δ_{pr}	variation of the preload displacement due to the displacement of actuator
$[\sigma]$	allowable stress
σ_{max}	maximum stress
θ_{ϕ_i}	rotational angle of ϕ_i
I_ψ	moment of inertia of ψ
$k_{\theta\phi}$	equivalent rotational stiffness of ϕ
k_k	equivalent input stiffness of the platform
k_{PPCA}	equivalent stiffness of the PPCA
k_{pr}	equivalent stiffness of the external preload mechanism
L_k	length of the link A_iB_i, B_iC_i, C_ip, A_ip, a_ib_i, b_ic_i, A_ic_i, C_iC_j and A_iA_j, k = 1, 2, 3, 4, 5, 6, 7, 8, 9, i, j = 1, 2, 3, $j \neq i$
l_k	dimensionless parameter of the length L_k, k = 1, 2, 3, 4
m_ψ	mass of ψ
Q_i	generalized non-conservative forces
q_i	linearly independent generalized coordinates
r_l	displacement loss factor of a lever amplifier
r_{l_b}	bending displacement loss factor of a lever amplifier
r_{l_d}	drift displacement loss factor of a lever amplifier
V_ψ	velocity of ψ
3RRR	3-revolute-revolute-revolute
disp.	displacement
DLM	displacement-loss model
DOF	degree of freedom
E	Young's modulus
F	force
I	flexure cross-sectional moment of inertia
M	bending moment
max	maximum
o	center of the fixed plate, origin of the coordinate system
p	center of the moving plate
PPCA	packaged piezoelectric ceramic actuator
PRBM	pseudo-rigid-body model
SGS	strain gauge sensor

a highly rigid platform with large magnification, two DLMs are essential in both the kinematic and dynamic models.

Because of the limited stroke provided by the PPCA, a displacement-magnifying mechanism is required to enlarge the workspace of the platform. In comparison with bridge-type amplifying mechanisms [14] and the Scott Russell mechanism [2,19,26], the commonly used lever amplifier is simple and efficient [10,27–32]. Scire and Teague [27] used a two-stage lever to obtain an output motion of about 68 μm. Piezoelectric actuators with a stroke of 2.25 μm produce an output of only around 38 μm. This motion loss is due to epoxy bonding and its coupling to the lever system, and to stretching of the flexure-hinge. Furukawa and Mizuno [28] utilised a planar eight-bar linkage to magnify the motion. The deflection of the input bars and the stretching of each flexure hinge were modelled in the design equations. Jouaneh and Yang [29] proposed a general approach for the design of flexure-hinge-type lever mechanisms. Min et al. [30] described an analytic lever model and its experimental verification. The PRBM approach was the basis of the analysis, kinematic and dynamic modelling, and experiments on compliant mechanisms. For levers with large magnification, the modelling error of the PRBM increases significantly. In the present study, a third DLM of the flexible lever mechanism is therefore proposed to compensate for losses in the PRBM.

2. Platform design

2.1. Design of a new external preload mechanism

The PPCA has a sub-millisecond response and generates a high-frequency motion. A high-frequency or large-amplitude nanoscale driving displacement is necessary for some micro/nano applications. The PPCA needs to maintain a constant connection status with the platform during the whole positioning procedure. Since extraneous lateral forces or moments may damage the PPCA, an appropriate external preload mechanism is essential for the desired PPCA movement in the axial direction. Shear stresses or large tensile stresses must not be directly applied to the PPCA.

Originally, traditional external PPCA preload mechanisms typically utilised two wedges to generate a thrust force [17], as shown in Fig. 1(a). Since the equivalent thrust force between two wedges is not in the axial direction, a lateral force or moment cannot be avoided and the initial preload displacement cannot be controlled directly. Although some special mechanisms may be used to adjust the downward displacement of one of the wedges with fine resolution, the forward displacement of the other wedge cannot be measured or controlled. The second typical preload mechanism uses a screw and a block [1,3,5,6,9,10,14,15,19,32], as shown in Fig. 1(b). Also in this case, the preload displacement cannot be measured, and a lateral force or moment is produced during the adjustment of the screw.

The preload displacement may vary greatly, especially during a long-term or high-frequency positioning procedure. A new external preload mechanism has been designed, as shown in Fig. 2. A steel ball is seated in a hemispherical cavity in the preload block. The interaction of the steel ball and the preload block precludes the generation of lateral force or moment. The ball eliminates torque during adjustment using the fine-tooth screw. A laser interferometer uses a reflector to measure any minute variation of the preload displacement that may occur.

2.2. Design of a two-level lever amplifier

The platform uses three two-level lever amplifiers to expand the workspace of the moving plate, as shown in Fig. 3.

The flexible lever with a high amplification ratio experiences bending deformation and pivot drifting. The traditional PRBM method would calculate a higher amplification ratio than the simulation or experiment. The analysis of the displacement loss is conducted in Section 3.

2.3. Optimization of the main design parameters

The 3-revolute-revolute-revolute (3RRR) parallel mechanism obtains high accuracy and precision, high rigidity and outstanding dynamic characteristics. This simple and convenient configuration has been widely applied in planar 3-DOF nanopositioning [7,9,12,13,16–20].

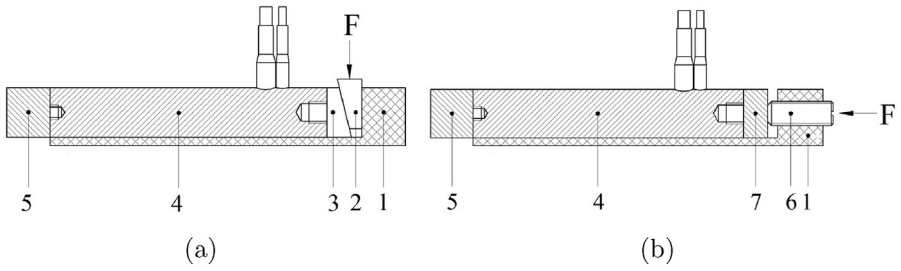

Fig. 1. Traditional external preload mechanism. The numbered components are: (1) fixed plate of the platform; (2) moving wedge; (3) fixed wedge; (4) PPCA; (5) moving plate of the platform; (6) screw; (7) preload block. *F* is the preload force.

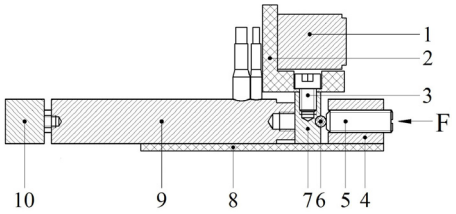

Fig. 2. Proposed external preload mechanism. The numbered components are: (1) laser interferometer reflector; (2) reflector support; (3) screw; (4) fixed platform plate; (5) fine-tooth screw; (6) steel ball; (7) preload block; (8) spacer for fixed plate; (9) PPCA; (10) input port of the platform. *F* is the preload force.

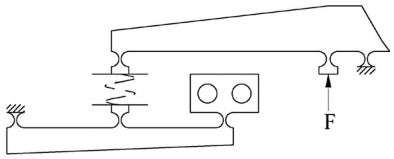

Fig. 3. Two-level lever amplifier.

For the proposed platform, the second-level lever A_iB_i (i = 1, 2, 3) acts as the master bar of the 3RRR mechanism. The slave bar is mounted on the master bar using a screw and a dowel pin. The moving plate is replaceable, as shown in Fig. 4(a).

The 3RRR mechanism has four design parameters and each of them can have any value between zero and infinity, as shown in Fig. 4(b). The conditioning index evaluates the velocity, accuracy and rigidity mapping characteristics between the input variables and the moving plate. The stiffness, payload and velocity index are also important for parallel platforms. The four objective functions are always highly non-linear and the optimization process is iterative and time consuming. An optimal result may be provided, but the user cannot know how optimal the result is. Using performance charts, the antagonism of multiple criteria can be identified globally. In order to present the performance chart in a finite space, it is necessary to normalize four design parameters.

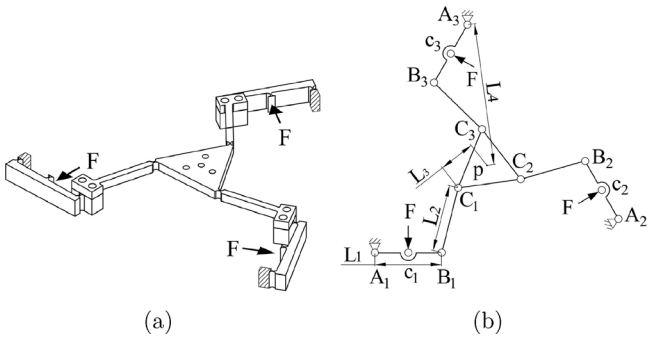

Fig. 4. 3RRR parallel mechanism.

Table 1
Optimised design parameters.

i	1	2	3	4
l_i	0.8563	0.8563	0.4676	1.8197
L_i (mm)	55.2	55.2	30.143	117.298

Table 2
Performance indices of the optimised dimensions.

Index	Conditioning	Stiffness	Payload	Velocity
Mean value	0.9995	0.1446	0.0229	51.9450
Standard deviation	0.0038	0.0005	0.00003	0.0713
Maximum value	1.0000	0.2702	0.0233	51.9668

$$l_i = \frac{L_i}{n_l} \tag{1}$$

where $n_l = (1/4)\sum_{i=1}^{4} L_i$.

Then the four design parameters can be converted into four dimensionless parameters. When the parameter normalization method is applied to mechanisms that have linear parameters, it can reduce parameter number, study a type of mechanism completely, remain performance similarity of mechanisms, and implement the optimal kinematic design in a limited parameter space [33]. Using the method provided in [24] and the optimization tool in MATLAB software, the optimised results are listed in Tables 1 and 2. Four dimensionless parameters can be translated into four dimensions with constant magnification.

2.4. Design of the very small rotational angular measurement

Three capacitive sensors are employed to measure the output displacements of the moving plate. The differential of two sensors arranged in a line are used to calculate the rotational angle because of the proportional relationship between them [10,11]. The principle of another calculation method for the very small rotational angle of the moving plate is shown in Fig. 5.

$$\left|d_2 d_2''\right| = \frac{2\left|Pd_2\right| \sin(\delta\theta/2)\cos\left(\theta_0 - (\delta\theta/2)\right)}{\cos\delta\theta} \tag{2}$$

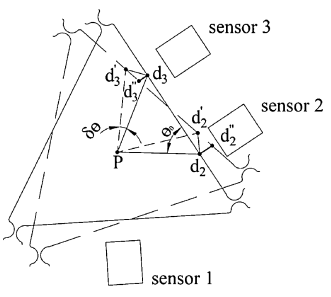

Fig. 5. Principle of the proposed method for measuring very small angles.

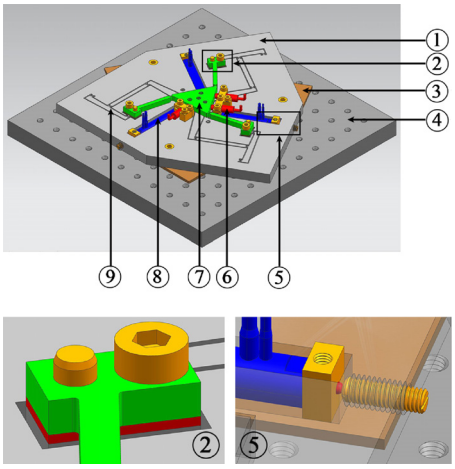

Fig. 6. Components of the platform: ① fixed plate; ② linkage unit of the master and slave bars; ③ washer of the fixed plate; ④ anti-vibration table; ⑤ preload mechanism; ⑥ capacitive displacement sensor; ⑦ moving plate; ⑧ PPCA; and ⑨ lever amplifier.

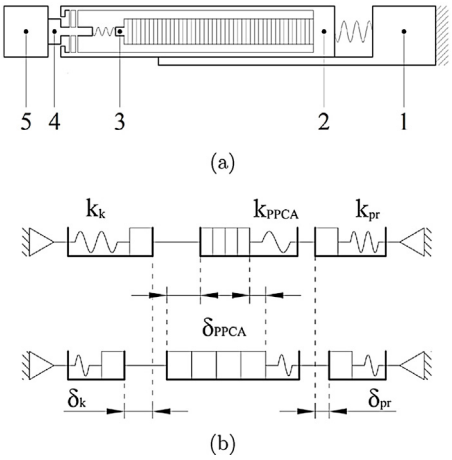

Fig. 7. Internal and external preload mechanisms of the PPCA. (a) Structural schematic diagram. The numbered components are: (1) fixed component; (2) PPCA casing; (3) output port of the multiple-layer piezoelectric stack; (4) output port of the PPCA; and (5) input port of the moving plate. (b) The dynamic model.

$$\left|d_3 d_3''\right| = \frac{2\left|Pd_3\right|\sin(\delta\theta/2)\cos(\theta_0 - (\delta\theta/2))}{\cos\delta\theta} \tag{3}$$

Eqs. (2) and (3) are derived from the sine rule to calculate very small angles. The translational displacements are calculated from the measured value of sensor 1 combined with the average measured values of sensors 2 and 3.

2.5. Overall design

The integral assembly diagram of the proposed platform is shown in Fig. 6. The platform has three symmetrical kinematic chains connecting the fixed plate and the moving plate. Twenty-one circular flexure hinges of rectangular cross-section act as revolute pairs. Various compliance/ stiffness calculation equations for circular flexure hinges were compared with FEA results in [34]. The related equations in [22] were selected to calculate the stiffness matrix of the flexure hinge.

3. Displacement loss modelling

The workspace of the moving plate depends on the actual input displacement of the platform and the actual amplification ratio, not the nominal displacement of the PPCA and the theoretical amplification ratio. The displacement loss occurs in the external preload port of the actuator, the input port of the platform, and the lever amplifier. These losses need to be investigated to compensate for the kinematic relationship between the SGSs and the moving plate. Three kinds of DLMs are proposed to compensate for the modelling errors in traditional systems.

3.1. Displacement loss in the external preload port

The PPCA comprises the multiple-layer piezoelectric stack. The integrated high-resolution SGS is used to measure the nominal displacement (i.e., the displacement of the PPCA without any load or external preload) of all the piezoelectric layers. Any decrease of external preload displacement is termed the displacement loss in the external preload port. Then the first DLM can be built.

Fig. 7 shows the analytical model of the preload port. The fixed component is the fixed plate and spacer. Generally, a PPCA may be seen as an equivalent mass-spring system. Then the equations for calculating the displacement loss in the preload port are written as

$$\delta_k k_k = \left(\delta_{PPCA} - \delta_k - \delta_{pr}\right) k_{PPCA} = \delta_{pr} k_{pr}, \tag{4}$$

$$\delta_{pr} = \frac{k_k k_{PPCA}}{k_{pr}k_k + k_{PPCA}k_k + k_{pr}k_{PPCA}}\delta_{PPCA}, \tag{5}$$

Eq. (5) shows that the displacement loss in the preload port depends on the equivalent input stiffness of the platform, the stiffness of the PPCA, and the stiffness of the external preload mechanism. The preload characteristics during the whole positioning procedure has a significant impact on the input displacement of the platform. Experimental testing of the first DLM along the single-axis and circle tracking is described in Section 5.

3.2. Displacement loss in the input port

The first DLM disappears if the stiffness of the external preload mechanism value is sufficiently large, but the load still generates a difference between the nominal displacement of the PPCA and actual input displacement of the platform. This difference is termed the displacement loss in the input port.

The second DLM is derived as follows: from Eq. (4), the input displacement of the platform is given by

$$\delta_k = \frac{k_{pr}k_{PPCA}}{k_k k_{pr} + k_{PPCA}k_{pr} + k_k k_{PPCA}}\delta_{PPCA}. \tag{6}$$

Eq. (6) shows that the actual input displacement of the platform is less than the nominal displacement of the PPCA. The equivalent stiffness of the PPCA depends mainly on the cross-sectional area of the PPCA, which depends on the size of the fixed plate. The equivalent input stiffness of the platform is subject to the natural frequency, workspace and dynamic performance.

3.3. Displacement loss of the flexible lever mechanism

The theoretical displacement amplification ratio of the two-level lever amplifier is obtained using the PRBM approach. When a load is attached, the lever mechanism experiences bending deformation and pivot drifting. The actual amplification ratio is then smaller than the theoretical ratio. This difference is termed the displacement loss of the lever. Both the bending deformation and pivot drifting are involved in the third DLM. Three flexure hinges produce

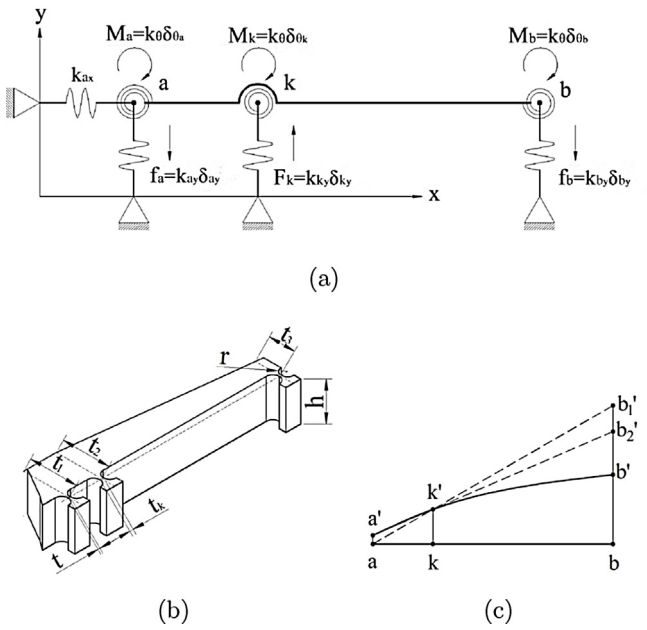

Fig. 8. First-level lever: (a) analysis model; (b) monolithic model; (c) bending schematic diagram.

a similar counter-moment when the lever rotates, which must be taken into account in the analytic lever model.

3.3.1. Bending beam model of the flexible lever mechanism

The analytical model of the first-level lever amplifier is shown in Fig. 8(a) and the 3D model in Fig. 8(b). The theoretical magnification ratio using the PRBM approach is $|ab| / |ak|$.

The actual bending schematic diagram is shown in Fig. 8(c). The length of $|b_2{}'b_1{}'|$ is the lost displacement caused by deformation of pivot a. The length of $|b'b_2{}'|$ is the lost displacement caused by the bending deformation of the flexible lever. Then r_l, r_{l_d} and r_{l_b} are defined as the displacement loss factor, the drift displacement loss factor, and the bending displacement loss factor of a lever amplifier, respectively, where

$$r_l = \left(\frac{|b'b_1{}'|}{|bb_1{}'|} \right) \times 100\%, \tag{7}$$

$$r_{l_d} = \left(\frac{|b'b_2{}'|}{|bb_1{}'|} \right) \times 100\%. \tag{8}$$

$$r_{l_b} = \left(\frac{|b_2{}'b_1{}'|}{|bb_1{}'|} \right) \times 100\%, \tag{9}$$

The force and moment equilibrium equations for pivot a are obtained using

$$f_a + f_b - F_k = 0, \tag{10}$$

$$M_a + M_k + M_b - F_k |ak| + f_b |ab| = 0. \tag{11}$$

Substituting $F_k = k_k \delta_{k_y}$ and $f_b = k_{b_y} \delta_{b_y}$ into Eq. (11) yields

$$\frac{\delta_{b_y}}{\delta_{k_y}} = \frac{\lambda_a k_k |ak| |ab|}{k_{\theta_a} + \lambda_k k_{\theta_k} + \lambda_b k_{\theta_b} + \lambda_a k_{b_y} |ab|^2}, \tag{12}$$

where $\lambda_a = \delta_{b_y} / (|ab| \delta_{\theta_a})$, $\lambda_k = \delta_{\theta_k} / \delta_{\theta_a}$ and $\lambda_b = \delta_{\theta_b} / \delta_{\theta_a}$.

If the input and output movements are assumed to be collinear, λ_k and λ_b are assumed to be 1. This assumption is proved in Section 4. It is obvious that the counter-moment of the flexure hinge at the displacement input point k and output point b cannot be ignored. $\lambda_{a'} = \delta_{k_y} / (|ak| \delta_{\theta_a})$ are defined in Fig. 8(c), such that Eq. (12) may be rewritten as

$$\frac{\delta_{b_y}}{\delta_{k_y}} = \frac{\lambda_{a'} k_k |ab|^2 - \left(k_{\theta_a} + \lambda_k k_{\theta_k} + \lambda_b k_{\theta_b} \right)}{\lambda_{a'} k_{b_y} |ak| |ab|}. \tag{13}$$

The deflection of the lever is given by

$$\ddot{\omega}(x) = \frac{M(x)}{EI(x)} \left(1 + \ddot{\omega}^2(x) \right)^{1.5} \approx \frac{M(x)}{EI(x)}. \tag{14}$$

where ω represents the deflection of the bending beam.

3.3.2. Finite element analysis of the flexible lever mechanism

A two-dimensional eight-node solid element was used to mesh the platform. Each node has two degrees of freedom in the x- and y- directions. Three screw holes in the fixed plate are also fixed, and all the DOFs are constrained. The deformation of the first-level lever amplifier along the y-axis is listed in Table 3 for different input displacements.

In Table 3, the displacement loss ratio of the first-level lever is as high as 26% because of the large amplification and load. The amplification of the first-level lever is 4.82. Eqs. (13) and (14) may be used to increase k_{a_y}, t_1, t_2, t_3 or h, or to decrease k_{b_y}, k_θ or k_{θ_k} to achieve a low displacement loss ratio.

The deformations of the second-level lever amplifier along the y-axis are given in Table 4 for different input displacements. Unlike the first-level lever, the displacement loss ratio of the second-level lever is about 5%, with small amplification and load. The comparison of theoretical calculation, simulation and prototype test on all three DLMs is conducted in Section 5.2.

Table 3
Displacement loss in the first-level lever amplifier.

Input disp./μm	5	10	15	20
Pivot/μm	0.073	0.166	0.230	0.258
Output disp./μm	24.116	48.280	72.417	96.468
r_{l_d}	1.235%	1.405%	1.297%	1.092%
r_{l_b}	24.562%	24.318%	24.429%	24.702%
r_l	25.797%	25.723%	25.726%	25.794%

4. Kinematic and dynamic modelling

4.1. Stiffness modelling

The analysis models of the platform are shown in Fig. 9. The platform is regarded as a flexible frame consisting of 18 flexible-beam elements, 21 flexure-hinge elements, and 1 triangle-frame element. The flexible-beam and flexure-hinge elements are denoted from 1 to 39 (as shown in Fig. 9(a)), and the nodes are denoted from 1 to 42 (as shown in Fig. 9(b)). The driving ports are denoted by node 1, 15, and 29. The output body is the triangle-frame element. The equation of motion is expressed as

$$\boldsymbol{K}\boldsymbol{x} = \boldsymbol{F}, \tag{15}$$

Table 4
Displacement loss in the second-level lever amplifier.

Input disp./μm	23.934	47.693	71.924	95.923
Pivot/μm/	0.048	0.109	0.150	0.181
Output disp./μm	45.660	91.167	136.640	182.420
r_{l_d}	0.100%	0.114%	0.104%	0.094%
r_{l_b}	4.512%	4.309%	4.907%	4.819%
r_l	4.613%	4.423%	5.011%	4.913%

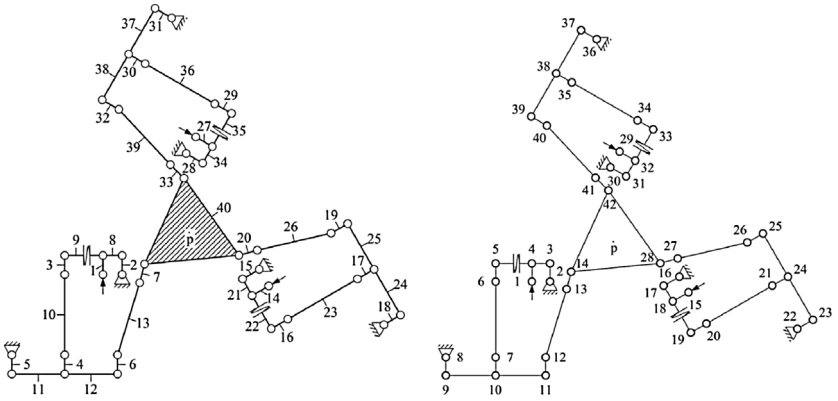

Fig. 9. Finite element model of the whole platform.

where $\boldsymbol{x}$ is given by

$$x = [\, q^{1T}, \quad \ldots \quad q^{iT}, \quad \ldots \quad q^{nT}, \,]^T \tag{16}$$

where n is the total number of nodes of the platform, and q^i is the displacement vector of the ith node, expressed as

$$q^i = [\, \Delta x_i \quad \Delta y_i \quad \Delta\theta_i \,]^T, \quad i = 1, 2, \ldots, n. \tag{17}$$

Considering the boundary conditions for the system, the 2nd, 8th, 16th, 22nd, 30th and 36th nodes are actually grounded. The Δx_i, Δy_i, and $\Delta\theta_i$ of Eq. (17) corresponding to these nodes should be set 0. The calculation methods of different element-stiffness-matrix can be found in [17,22]. The input stiffness of the platform is then calculated by solving Eq. (15).

4.2. Kinematic modelling

From the kinematic point of view, a rectangular circular flexure hinge generates rotation about one axis as an ideal revolute pair [20]. Then the equivalent PRBM of the whole platform can be simply built, as shown in Fig. 10. The origin of the coordinate system is located at the centre of the fixed plate, which is coincident with the centre of the moving plate in the initial status.

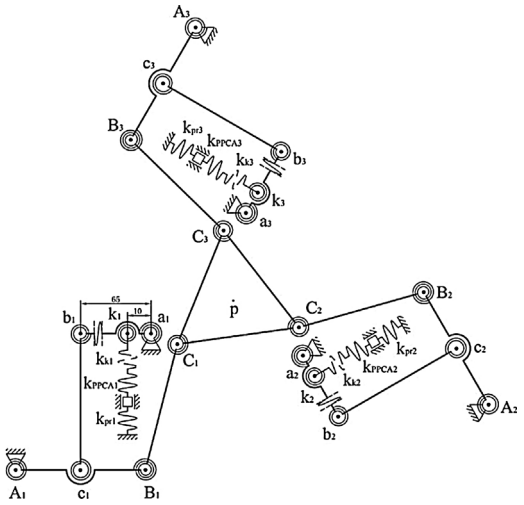

Fig. 10. Equivalent PRBM of the whole platform.

Based on the geometrical relationship of the two-level lever amplifier, the closed-loop geometrical constraint equations are expressed as

$$L_5 \cos\left(-\overline{\delta_{\theta_a}}\right) + L_6 \cos\delta_{\theta_{bc}} + L_7 \cos\overline{\delta_{\theta_A}} = L_5 + L_7, \tag{18}$$

$$L_5 \sin\left(-\overline{\delta_{\theta_a}}\right) + L_6 \sin\delta_{\theta_{bc}} + L_7 \sin\overline{\delta_{\theta_A}} = L_6, \tag{19}$$

where $\delta_{\theta_{bc}} = \pi/2 - \delta_{\theta_b} - \overline{\delta_{\theta_a}} = \pi/2 - \delta_{\theta_c} + \overline{\delta_{\theta_A}}$, $\overline{\delta_{\theta_a}} \approx \delta_{\theta_a}$ and $\overline{\delta_{\theta_a}} \approx \delta_{\theta_a}$. For a very small rotational angle δ_θ, $\cos\delta_\theta \approx 1$ and $\sin\delta_\theta \approx \delta_\theta$.

Based on the geometrical and motion relationship of the 3-RRR mechanism, the total kinematic relationship is given by

$$J_{p'}\dot{\vec{p}} = J_{\theta_A}\dot{\vec{\theta}}_A, \tag{20}$$

where $\dot{\vec{p}}$ and $\dot{\vec{\theta}}_A$ are defined as

$$\dot{\vec{p}} = \begin{pmatrix} \dot{x}_p & \dot{y}_p & \dot{\theta}_p \end{pmatrix}, \tag{21}$$

$$\dot{\vec{\theta}}_A = \begin{pmatrix} \dot{\theta}_{A_1} & \dot{\theta}_{A_2} & \dot{\theta}_{A_3} \end{pmatrix}. \tag{22}$$

The forward-kinematic Jacobian matrix J is given by

$$J = \frac{J_{\theta_A}}{J_{p'}}. \tag{23}$$

With the forward-kinematic analysis of the platform, the relationship between the input displacement of platform and the planar coordinate of the moving plate can be derived. From Eq. (23), every position in the workspace of the moving plate has a corresponding but different Jacobian matrix J.

4.2.1. Maximum stress analysis

When a pure bending moment acts on a bar around its axis of rotation, the maximum stress $\sigma_{\max}$ caused by the rotation occurs at the thinnest part of the flexure hinge. The method in [22] may then be used to calculate the $\sigma_{\max}$.

The maximum rotational angle of the 21 hinges are given by Eqs. (18)–(23) and the loop closure theory in [16]. For this platform, $\sigma_{\max}$ = 107.07 MPa< $[\sigma]$ = 228.79 MPa.

4.3. Dynamic analysis

Substituting the kinematic and potential energies into the Lagrange equation yields

$$\boldsymbol{M}\begin{bmatrix} \ddot{x}_p & \ddot{y}_p & \ddot{\theta}_p \end{bmatrix}^T + \boldsymbol{K}\begin{bmatrix} x_p & y_p & \theta_p \end{bmatrix}^T = \begin{bmatrix} Q_1^{(3)} & Q_2^{(3)} & Q_3^{(3)} \end{bmatrix}^T. \tag{24}$$

The natural frequencies are calculated from the total equivalent mass-stiffness matrix.

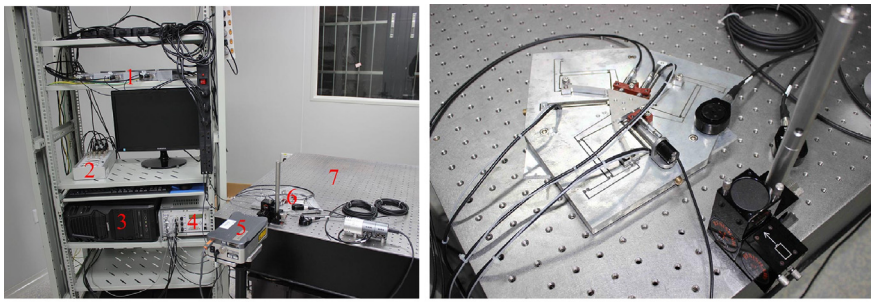

(a) (b)

Fig. 11. (a) Test setup of positioning system. Numbered components are: (1) capacitive sensor controller; (2) dSPACE; (3) PC; (4) PPCA controller; (5) laser interferometer; (6) 3-DOF platform; and (7) anti-vibration table. (b) Test setup of platform.

5. Experimental results and discussion

5.1. Experiment setup

5.1.1. Prototype fabrication

The wire electrical discharge machining technique (wire EDM) was used to manufacture the platform to maximise geometrical precision and uniform stiffness. The material of both the fixed and moving plates was aluminium alloy AA7075-T651, which has high elasticity, high yield strength, and light mass. The supports of the three capacitive sensors were made from Invar steel, which has the lowest coefficient of thermal expansion among metals. This allowed the sensors to be kept in an approximately constant position in a Class 10,000 clean-room (ISO 7 standard, ISO 14644-1).

An overview of the experimental setup and platform are shown in Fig. 11. Three PPCAs (P-841.30, from PI Ceramic GmbH) with a closed-loop stroke of 45 μm were selected to drive the platform. These have static stiffness 19 N/μm ±20%; the dynamic stiffness for small signals is 19 N/μm ±30%. Three single-probe capacitive displacement sensors (D-E20 200, from PI Ceramic GmbH) were used to measure the output displacement of the moving plate. A single-board controller board (DS1104, from dSPACE GmbH) was used for data acquisition from the three capacitive sensors and the three SGSs. The board was able to be configured as either a semi-closed-loop or a closed-loop controller. All of the above instruments were mounted onto an anti-vibration table (AYA-1510K4, from Newport Corporation). A laser interferometer (XL-80, from Renishaw Inc.) was used to measure the variation of the preload displacement or the moving plate.

5.2. Experimental validation of the three DLMs

5.2.1. Validation of the first DLM

Firstly, the experiment on the first DLM was conducted along a single axis. The position of the preload block reflects the variation of the preload displacement. A reflector was mounted on the preload block, and a laser interferometer was used to measure the variation. The driving signal is either step voltage in the open-loop mode, or a step displacement in the semi-closed-loop mode. The signal steps ranged from zero to the maximum value and then from maximum value to zero. When the other two PPCAs are preloaded, the coupling effect influenced the preload displacement of the first PPCA. A selection of experimental results are shown in Fig. 12.

The PPCA showed hysteresis in the open-loop mode, and possessed a linear displacement in the semi-closed-loop mode. The variation of the preload displacement had the same characteristic, whether or not the other two PPCAs were preloaded; that is, the preload characteristic depended primarily on the corresponding PPCA. Maximum variation was about 12.2–16.6% of the maximum nominal displacement of the PPCA. The coupling effect reduced the variation of the corresponding preload displacement.

5.2.2. Validation of the second and third DLMs

In order to examine the second and the third DLMs, a micro-vision measuring system was used to obtain the moving displacement at multiple points of the platform. The experimental system is shown in Fig. 13.

The nominal maximum displacement of the PPCA is 45 μm. A loop is defined as an displacement of 0–45–0 μm with a step of 5 μm. Nineteen figures can be obtained in a loop using the micro-vision measuring system and numbered from 0 to 18. Seven of them are shown in Fig. 14.

A template was selected to calculate the moving displacement of the next figure relative to the previous figure. According to the template matching method, eighteen corresponding displacements at point k_1, b_1, c_1, and B_1 were calculated. The results are shown in Fig. 15.

The point b_1 is used to represent the output displacement of the first lever and point c_1 represents the input displacement of the second lever. The link b_ic_i ($i = 1, 2, 3$) has a length of 58.0 mm and a cross section of 4.6 mm × 12.0 mm. The link may be stretched during the motion. The difference between the point b_1 and c_1 can be

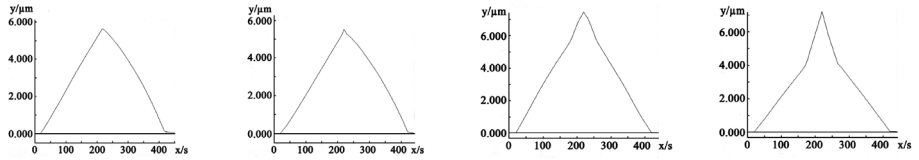

(a) Open-loop, 5.644 μm (b) Open-loop & coupling, 5.494 μm (c) Semi-closed-loop, 7.460 μm (d) Semi-closed-loop & coupling, 7.201 μm

Fig. 12. Variation in external preload displacement.

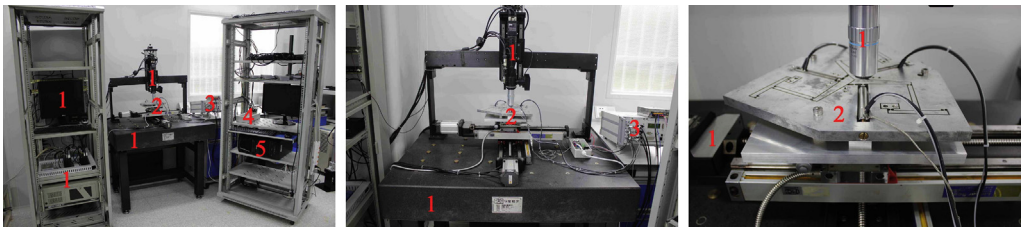

Fig. 13. Test setup for the DLMs. Numbered components are: (1) micro-vision measuring system; (2) proposed platform; (3) PPCA controller; (4) dSPACE; and (5) PC.

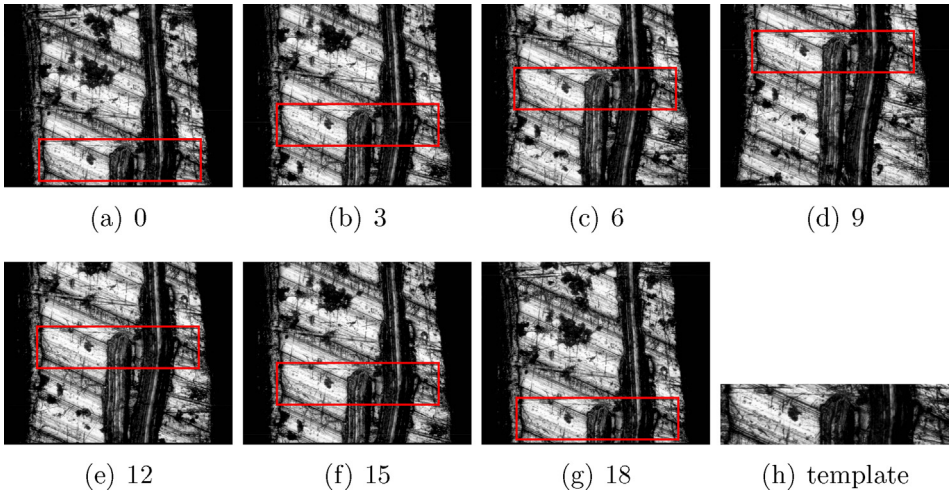

Fig. 14. Seven figures during a loop and the common template of the whole 19 figures.

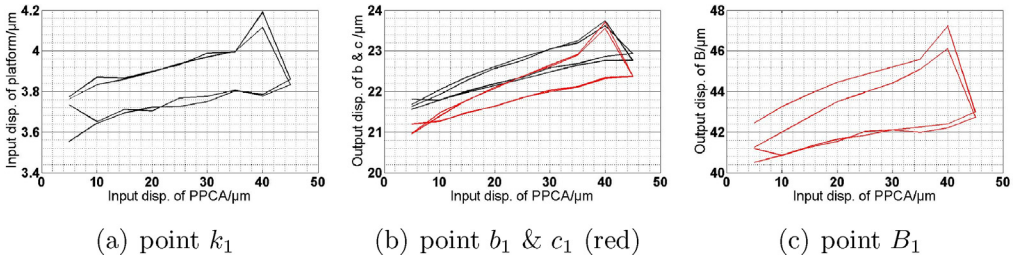

Fig. 15. Moving displacement at point k_1, b_1, c_1, and B_1.

obtained using the theoretical calculation and simulation, as shown in Tables 3 and 4. The experimental validation of the difference is shown in Fig. 15(b).

$\delta_{pr}/\delta_{PPCA}$ and δ_k/δ_{PPCA} are used to calculate the percentage displacement loss of the first DLM and the second DLM, respectively. The experimental results were compared with theoretical calculation and simulation results to examine the three DLMs. The results are shown in Table 5.

Three DLMs have been validated to possess a large value. The use of three DLMs can improve the modelling and experimental accuracy. Three losses may also be an important factor needing to be considered in the process of designing or controlling a nanopositioning platform with large magnification.

Table 5
Displacement loss on three DLMs (%).

Items	First DLM	Second DLM	Third DLM		
			1st	2nd	Total
Calculation	15.43	35.08	20.92	14.00	32.00
Simulation	15.23	34.64	25.85	5.50	29.92
Test	16.22[a]	25.49	9.54	7.00	15.87

[a] The value came from the test with the semi-closed-loop controller.

5.3. Kinematic and dynamic test

Three PPCAs have an nominal maximum displacement of 45 μm using the semi-closed-loop controller. Firstly, three PPCAs possessed zero displacement. A driving step-displacement signal of 0–45 μm and 45–0 μm with a step of 3 μm was applied to the first PPCA. When the first PPCA completed a loop of 0–45 μm or 45–0 μm, the second PPCA added 3 μm; when the second PPCA completed a loop of 0–45 μm, the third PPCA added 3 μm. Then the actual workspace of the moving plate was obtained after the third PPCA completed a loop of 0–45 μm, as shown in Fig. 16.

A laser interferometer measured the output step of the moving plate. Actual resolutions of the moving plate were acquired, as shown in Fig. 17.

A portable modal testing system (Zonicbook/618E, from IOtech Inc.) was used to perform modal analysis of the platform. The natural frequency was compared with the theoretical calculation, simulation, and prototype test, to examine the dynamic model. The results are shown in Table 6.

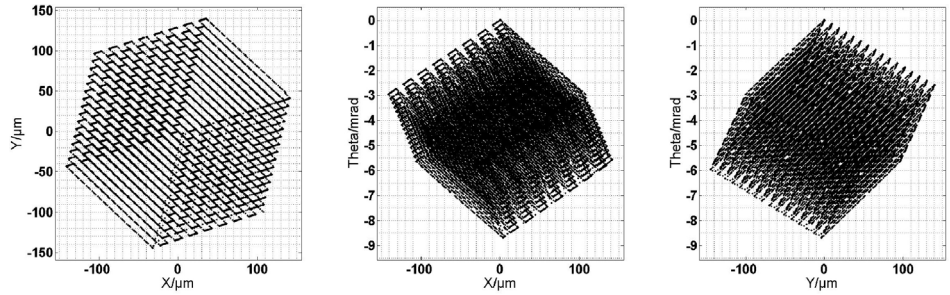

Fig. 16. Actual workspace of the moving plate.

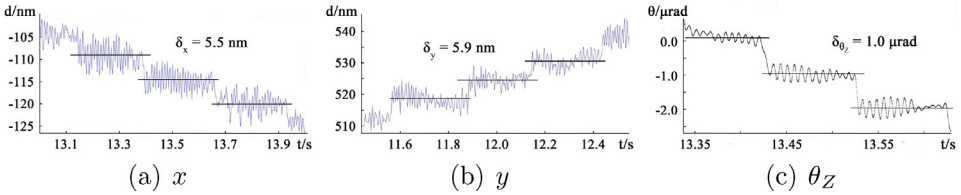

Fig. 17. Actual resolutions of the moving plate.

Table 6
Comparative results of theoretical calculation, simulation and prototype test.

Items	Workspace			Frequency/Hz		
	x/μm	y/μm	θ_Z/mrad	1st	2nd	3rd
Calculation	217.75	219.02	7.01	280.38	280.48	379.56
Simulation	230.97	232.32	7.18	301.14	316.24	419.65
Test	283.13	284.78	8.73	243.09	243.09	405.52

Table 7
Circular tracking results using the semi-closed-loop controller.

Velocity (μm/s)	1	2	4	8
Tracking accuracy (nm)	24.0	7.5	28.5	35.7
Tracking precision (nm)	49.8	57.4	92.1	197.4
Homing accuracy (nm)	114.8	53.0	37.9	19.7
1st DLM (nm)	793	793	794	783

5.4. Circular trajectory tracking

5.4.1. Semi-closed-loop controller

Three DLMs were used to compensate for the kinematic relationship of the platform. The moving plate tracked a 50 μm-diameter circular path at different speeds. Three capacitive sensors are used to measure the actual position of the moving plate with a sampling frequency of 1.24 kHz. The corresponding tracking errors are shown in Fig. 18 and the preload displacements are shown in Fig. 19.

The preload displacement varied as long as the PPCA functioned, and directly reduced the actual input displacement. The circle tracking results are shown in Table 7. Tracking accuracy and precision are respectively represented by the mean error and the mean square error of the actual tracked radius compared to the desired trajectory. "Homing accuracy" refers to the mean error between the starting point and the end point of the circle. 1st DLM represents the maximum variation of the preload displacement.

In Table 7, the platform shows a high positioning accuracy and precision at different speeds along a 50 μm-diameter circular

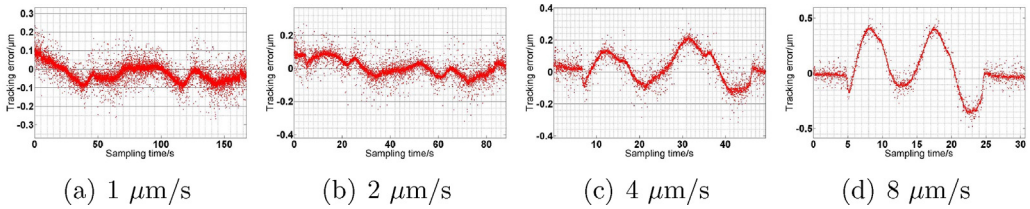

Fig. 18. Tracking error of the moving plate with a semi-closed-loop controller.

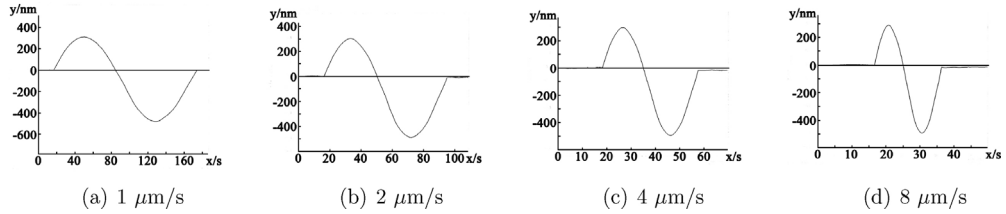

Fig. 19. The external preload displacement of one PPCA.

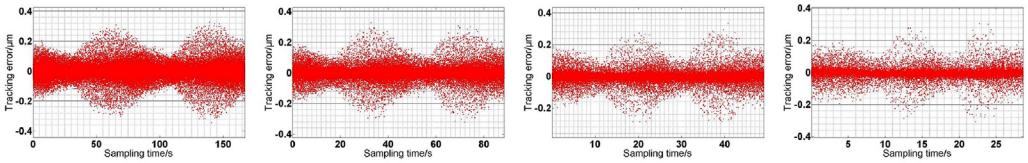

(a) 1 μm/s (b) 2 μm/s (c) 4 μm/s (d) 8 μm/s

Fig. 20. Tracking error of the moving plate with a closed-loop controller

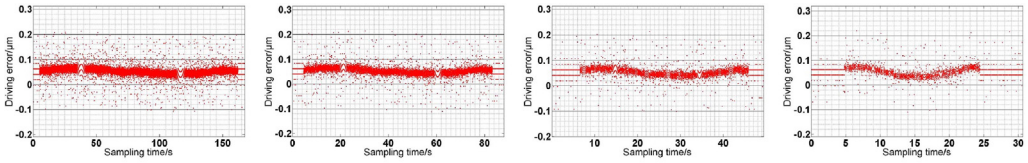

(a) 1 μm/s (b) 2 μm/s (c) 4 μm/s (d) 8 μm/s

Fig. 21. Driving error of one PPCA with a semi-closed-loop controller.

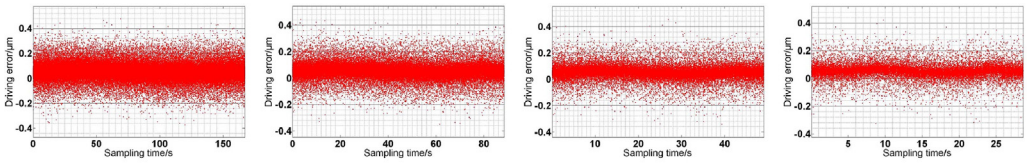

(a) 1 μm/s (b) 2 μm/s (c) 4 μm/s (d) 8 μm/s

Fig. 22. Driving error of one PPCA with a closed-loop controller.

trajectory, with a tracking accuracy of 7.5 nm at 2 μm/s and a homing accuracy of 19.7 nm at 8 μm/s.

The semi-closed-loop controller could not measure the actual input displacement of the platform. It is difficult to compensate for variation in the preload displacement. The error decreased the positioning accuracy and precision significantly.

5.4.2. Closed-loop controller

A PID controller based on three capacitive sensors and three SGSs was constructed. The controller had a closed-loop feedback for the moving plate and the other feedback for the PPCA. The moving plate tracked a 50 μm-diameter circular trajectory at different speeds. The controller gains of the PID controller were set at $k_p = 1.2$, $k_i = 100$, and $k_d = 0.005$. The results are shown in Fig. 20.

Figs. 18 and 20 show that the tracking accuracy decreased as tracking velocity increased. High-speed tracking plays an important role in nanopositioning fields such as the atomic force microscope (AFM). Conversely, the closed-loop controller tracking performed was highly accurate at all speeds. For comparison, the driving errors using the semi-closed-loop controller and closed-loop controller are shown in Figs. 21 and 22.

Both controllers utilised the SGS to control the PPCA. With the semi-closed-loop controller, the PPCA could not track the desired trajectory when the driving harmonic signal reached a maximum or minimum value. The difference between the actual displacement and the desired value of the PPCA would be magnified by the lever and further decrease the tracking accuracy. Lower speeds produced larger accumulated errors. Conversely, with the closed-loop controller, the PPCA maintained a high tracking accuracy at different speeds.

Table 8 shows that the tracking accuracy on a 50 μm-diameter circular trajectory was less than 5 nm and the homing accuracy was less than 1 nm. The tracking precision during the whole positioning procedure was about 40 nm.

Table 8
Circle tracking results with the closed-loop controller.

Velocity (μm/s)	1	2	4	8
Tracking accuracy (nm)	0.8	1.6	2.9	4.4
Tracking precision (nm)	40.5	39.4	39.6	39.9
Homing accuracy (nm)	0.05	0.16	0.71	0.21
1st DLM (nm)	740	738	734	745

5.5. Discussion

The PPCA has an nominal displacement of 45 μm and static stiffness of 19 ± 20% N/μm. An actual workspace of 283.13 μm × 284.78 μm × 8.73 mrad was achieved. A PPCA with a larger stroke or a higher stiffness could be used if a larger workspace was required.

The use of three DLMs not only improved the modelling accuracy and the tracking accuracy and precision, but also indicated other possibilities for further increasing the magnification. Increasing the preload stiffness reduces the loss in the first DLM. The PPCA with high stiffness or high driving voltage would reduce the loss in the second DLM. The material, dimension and cross-sectional area of the flexible lever can be optimised to minimise the loss in the third DLM.

The input stiffness of the platform mainly depends on the magnification of the lever mechanism and the stiffness of the 21 hinges. The input stiffness has a significant effect on the loss in the second DLM and the natural frequency.

The semi-closed-loop controller imposes strict requirements on both the modelling accuracy and the accuracy of manufacture, the latter being difficult to compensate for. The closed-loop controller would be an effective proposal.

6. Conclusions

This paper presents the design, modelling and experimental investigation of a planar parallel 3-DOF nanopositioning platform.

A new preload mechanism design is proposed to validate the first DLM for the first time. Three two-level lever amplifiers are arranged symmetrically to achieve large magnification. The parallel-kinematic configuration with optimal sizes increases the rigidity. Three DLMs are proposed, and on this basis a more accurate kinematic and dynamic model of the platform is derived. The experimental results show that the proposed platform produces large magnification with high-precision circle tracking and high-accuracy positioning. The main contribution of this study is the design and modelling methods of a planar 3-DOF nanopositioning platform. There would always be a trade-off between compact structure, high rigidity, large magnification, high-precision tracking, and high-accuracy positioning. The proposed design and modelling methods provide an effective and competitive solution.

Future research will focus on applying different intelligent control strategies to improve the positioning precision, trajectory tracking accuracy and dynamic performance at a higher velocity.

Acknowledgements

This research was supported by the Scientific and Technological Research Project of Guangdong Province (2014B090917001, 2015B020239001), the National Natural Science Foundation of China (Grant Nos. U1501247, 91223201), and the Natural Science Foundation of Guangdong Province (Grant No. S2013030013355). This support is greatly acknowledged.

References

Yong, Y.K., Aphale, S.S., Moheimani, S.O.R., 2009. Design, identification, and control of a flexure-based xy stage for fast nanoscale positioning. IEEE Trans Nanotechnol 8 (1), 46–54, http://dx.doi.org/10.1109/TNANO.2008.2005829.

Hwang, D., Lee, M.G., Jeong, J., 2011. Note: Design of a novel ultraprecision in-plane xyθ positioning stage. Rev Sci Instrum 82 (8), http://dx.doi.org/10.1063/1.3516042, 026102–026102-3.

Yong, Y.K., Moheimani, S.O.R., Kenton, B.J., Leang, K.K., 2012. Invited review article: high-speed flexure-guided nanopositioning: mechanical design and control issues. Rev Sci Instrum 83 (12), http://dx.doi.org/10.1063/1.4765048, 121101–121101-22.

Tang, H., Li, Y., 2013. Design, analysis, and test of a novel 2-DOF nanopositioning system driven by dual mode. IEEE Trans Robot 29 (3), 650–662, http://dx.doi.org/10.1109/TMECH.2011.2166162.

Qin, Y., Shirinzadeh, B., Tian, Y., Zhang, D., Bhagat, U., 2014. Design and computational optimization of a decoupled 2-DOF monolithic mechanism. IEEE/ASME Trans Mechatron 19 (3), 872–881, http://dx.doi.org/10.1109/TMECH.2013.2262801.

Ryu, J.W., Gweon, D.-G., Moont, K.S., 1997. Optimal design of a flexure hinge based xyθ wafer stage. Precis Eng 21 (1), 18–28, http://dx.doi.org/10.1016/S0141-6359(97)00064-0.

de Jong, B.R., Brouwer, D.M., de Boer, M.J., Jansen, H.V., Soemers, H.M.J.R., Krijnen, G.J.M., 2010. Design and fabrication of a planar three-DOFs MEMS-based manipulator. J Microelectromech Syst 19 (5), 1116–1130, http://dx.doi.org/10.1109/JMEMS.2010.2067196.

Tian, Y., Shirinzadeh, B., Zhang, D., Liu, X., Chetwynd, D., 2009. Design and forward kinematics of the compliant micro-manipulator with lever mechanisms. Precis Eng 33 (4), 466–475, http://dx.doi.org/10.1016/j.precisioneng.2009.01.003.

Tian, Y., Shirinzadeh, B., Zhang, D., 2010. Design and dynamics of a 3-DOF flexure-based parallel mechanism for micro/nano manipulation. Microelectron Eng 87 (2), 230–241, http://dx.doi.org/10.1016/j.mee.2009.08.001.

Bhagat, U., Shirinzadeh, B., Clark, L., Chea, P., Qin, Y., Tian, Y., et al., 2014. Design and analysis of a novel flexure-based 3-DOF mechanism. Mech Mach Theory 74, 173–187, http://dx.doi.org/10.1016/j.mechmachtheory.2013.12.006.

Chen, K.-S., Trumper, D., Smith, S., 2002. Design and control for an electromagnetically driven xyθ stage. Precis Eng 26 (4), 355–369, http://dx.doi.org/10.1016/S0141-6359(02)00147-2.

Chang, S.H., Tseng, C.K., Chien, H.C., 1999. An ultra-precision xyθ_z piezo-micropositioner. Part I: Design and analysis. IEEE Trans Ultrason Ferroelectr Freq Control 46 (4), 897–905, http://dx.doi.org/10.1109/58.775656.

Chang, S.H., Tseng, C.K., Chien, H.C., 1999. An ultra-precision xyθ_z piezo-micropositioner. Part II: Experiment and performance. IEEE Trans Ultrason Ferroelectr Freq Control 46 (4), 906–912, http://dx.doi.org/10.1109/58.775657.

Kim, H., Gweon, D.-G., 2012. Development of a compact and long range xyθ_z nano-positioning stage. Rev Sci Instrum 085102 (83), http://dx.doi.org/10.1063/1.4740254, 085102–8.

Ryu, J.W., Leea, S.-Q., Gweona, D.-G., Moon, K.S., 1999. Inverse kinematic modeling of a coupled flexure hinge mechanism. IEEE/ASME Trans Mechatron 9 (6), 657–674, http://dx.doi.org/10.1016/S0957-4158(99)00006-9.

Yong, Y.K., Lu, T.-F., Handley, D.C., 2004. Loop closure theory in deriving linear and simple kinematic model for a 3 DOF parallel micromanipulator. Proc SPIE 5276, 57–66, http://dx.doi.org/10.1117/12.22258.

Wang, H., Zhang, X., 2008. Input coupling analysis and optimal design of a 3-DOF compliant micro-positioning stage. Mech Mach Theory 43 (4), 537–547, http://dx.doi.org/10.1016/j.mechmachtheory.2007.04.009.

Yong, Y.K., Lu, T.-F., 2009. Kinetostatic modeling of 3-RRR compliant micro-motion stages with flexure hinges. Mech Mach Theory 44 (6), 1156–1175, http://dx.doi.org/10.1016/j.mechmachtheory.2008.09.005.

Qin, Y., Shirinzadeh, B., Zhang, D., Tian, Y., 2013. Design and kinematics modeling of a novel 3-DOF monolithic manipulator featuring improved Scott–Russell mechanisms. J Mech Des 135 (10), 1004–1009, http://dx.doi.org/10.1115/1.4024979.

Tahmasebi, F., 2007. Kinematics of a new high-precision three-degree-of-freedom parallel manipulator. J Mech Des 129, 320–325, http://dx.doi.org/10.1115/1.2406103.

Howell, L.L., 2001. Compliant Mechanisms. Wiley-Interscience, New York, NY, USA.

Lobontiu, N., 2003. Compliant Mechanisms: Design of Flexure Hinges. CRC Press, Boca Raton, FL, USA.

Gosselin, C., Angeles, J., 1988. The optimal kinematic design of a planar three-degreeof-freedom parallel manipulator. J Mech Des 110 (1), 35–41, http://dx.doi.org/10.1115/1.3258901.

Wu, J., Wang, J., Wang, L., You, Z., 2010. Performance comparison of three planar 3-DOF parallel manipulators with 4-RRR, 3-RRR and 2-RRR structures. Mechatronics 20 (4), 510–517, http://dx.doi.org/10.1016/j.mechatronics.2010.04.012.

Aderiaens, H., Koning, W., Baning, R., 2000. Modeling piezoelectric actuators. IEEE/ASME Trans Mechatron 5 (4), 331–341.

Chang, S.H., Du, B.C., 1998. A precision piezodriven micropositioner mechanism with large travel range. Rev Sci Instrum 69 (4), 1785–1791, http://dx.doi.org/10.1063/1.1148842.

Scire, F.E., Teague, E.C., 1978. Piezodriven 50-μm range stage with subnanometer resolution. Rev Sci Instrum 49 (12), 1735–1740, http://dx.doi.org/10.1063/1.1135327.

Mizuno, E., Mizuno, M., 1990. Displacement amplification and reduction by means of linkage. Bull Jpn Soc Precis Eng 24 (4), 285–290.

Jouaneh, M., Yang, R., 2003. Modeling of flexure-hinge type lever mechanisms. Precis Eng 27 (4), 407–418, http://dx.doi.org/10.1016/S0141-6359(03)00045-X.

Min, K.S., Choi, W.C., Song, S.H., Hwang, E.J., 2005. Static and dynamic analysis of a nanopositioning flexure-hinge stage with a flexible lever mechanism. Proc Inst Mech Eng B: J Eng Manuf 219 (6), 447–454, http://dx.doi.org/10.1243/095440505X32355.

Jianying, S., Qinghua, Z., 2006. Displacement loss of flexure-hinged amplifying mechanism. In: IMACS multiconference on computational engineering in systems applications, Beijing, China, pp. 1864–1867, http://dx.doi.org/10.1109/CESA.2006.313617.

Tang, H., Li, Y., 2012. Optimal design of the lever displacement amplifiers for a flexure-based dual-mode motion stage. In: 2012 IEEE/ASME international conference on advanced intelligent mechatronics (AIM), Kaohsiung, Taiwan, pp. 753–758, http://dx.doi.org/10.1109/AIM.2012.6265879.

Liu, X.-J., Wang, J., 2007. A new methodology for optimal kinematic design of parallel mechanisms. Mech Mach Theory 42 (9), 1210–1224, http://dx.doi.org/10.1016/j.mechmachtheory.2006.08.002.

Yong, Y.K., Lu, T.-F., Handley, D.C., 2008. Review of circular flexure hinge design equations and derivation of empirical formulations. Precis Eng 32 (2), 63–70, http://dx.doi.org/10.1016/j.precisioneng.2007.05.002.